Research Square

Preprints are preliminary reports that have not undergone peer review.
They should not be considered conclusive, used to inform clinical practice,
or referenced by the media as validated information.

Three-Dimensional Flame-Head Bifurcation and Compression– Hydrodynamic Coupling in LES of Premixed Hydrogen-Air Propagation in a Half-Open Channel

Youquan Yuan

[redacted]

Jiandong He

hjd@imut.edu.cn

[redacted]

Research Article

Keywords: hydrogen-air flame, large-eddy simulation, half-open channel, flame-head bifurcation, ahead-of-flame compression, precursor pathway

Posted Date: May 7th, 2026

DOI: https://doi.org/10.21203/rs.3.rs-9517192/v1

License: This work is licensed under a Creative Commons Attribution 4.0 International License.
Read Full License

Additional Declarations: No competing interests reported.

Three-Dimensional Flame-Head Bifurcation and Compression–Hydrodynamic Coupling in LES of Premixed Hydrogen-Air Propagation in a Half-Open Channel

Youquan Yuan[1] and Jiandong He[1*]

[1]College of Mechanics and Aerospace, Inner Mongolia University of Technology, Hohhot, Inner Mongolia, China.

*Corresponding author(s). E-mail(s): hjd@imut.edu.cn;

Abstract

Large-eddy simulations were used to examine premixed hydrogen-air flame propagation in a three-dimensional half-open channel. The stoichiometric mixture was taken as the reference condition, and neighboring lean and rich mixtures were introduced to test whether changes in equivalence ratio alter the pathway itself or mainly shift its onset and late-stage strength. In all three cases, wall confinement quickly suppresses the initial quasi-spherical kernel expansion and reorganizes the flame into a spanwise-stratified front, with the clearest head bifurcation on the center plane. Within a common LES closure, four coupled precursor quantities are tracked: flame-head bifurcation, ahead-of-flame compression, tip-center velocity separation, and wake backflow. The rich case enters the coupled precursor regime earliest in absolute time, whereas the stoichiometric case reaches the strongest late-stage structural-compressive state at matched normalized stages. These results support a single confinement-organized precursor pathway in which equivalence ratio mainly shifts entry timing and late-stage amplification rather than introducing a different mechanism. A late-stage collapse of the adaptive time step is observed near termination, but it is treated here as a secondary interpretive issue rather than as a primary mechanism claim.

Keywords: hydrogen-air flame; large-eddy simulation; half-open channel; flame-head bifurcation; ahead-of-flame compression; precursor pathway

1 Introduction

Hydrogen deflagration in ducts, channels, and partially vented enclosures remains a major safety concern because confinement couples heat release, pressure rise, and flow reorganization. Experimental and numerical studies in rectangular channels and semi-open configurations have shown that even moderate variations in geometry or mixture strength can materially alter flame morphology, overpressure, and propagation speed (Shen et al. 2021; Wang et al. 2024a; Sheng et al. 2024). Confined hydrogen-air propagation therefore provides a canonical configuration in which the coupled effects of geometry, compression, and hydrodynamics can be examined in a controlled manner.

Beyond integral measures such as flame speed and overpressure, confined premixed flames may develop finger-like fronts, tulip or distorted-tulip structures, centerline recession, and pronounced pressure–flame interaction. Classical studies attributed these behaviors to wall effects, no-slip-induced acceleration, flow reversal, and broader hydrodynamic reorganization (Akkerman et al. 2006; Bychkov et al. 2007; Ponizy et al. 2014; Qian and Liberman 2023). More recent hydrogen-air studies have further shown that confinement geometry exerts a strong influence on flame morphology, three-dimensional front structure, and flow reorganization (Liberman et al. 2023; Shen et al. 2023; Han et al. 2024; Shen et al. 2025; Liu et al. 2026). Studies of non-uniform or concentration-varied hydrogen-air mixtures likewise indicate that mixture strength can shift flame development and pressure response (Qu et al. 2024; Cao et al. 2024; Wang et al. 2025). What remains lacking, however, is a compact three-dimensional description that simultaneously resolves flame deformation, local compression loading, and velocity redistribution within a single half-open configuration.

Recent LES and combined experimental-numerical studies further indicate that confined hydrogen-flame dynamics cannot be inferred from flame shape alone, because front evolution is accompanied by coupled changes in pressure response and flow-field reorganization (Xu et al. 2024; Jiang et al. 2024b; Qu et al. 2025). Recent contributions in Flow, Turbulence and Combustion have clarified how wall configuration, wall thermal conditions, and near-wall transport reorganize reacting-flow structure during flame-wall interaction, especially in low-Reynolds-number boundary-layer settings (Ahmed et al. 2023; Ahmed et al. 2024). Those studies mainly address local near-wall turbulence and transport behavior. The present work extends the wall-effect question to a different configuration and scale, namely a three-dimensional half-open hydrogen-air channel in which confinement reorganizes not only the near-wall flow, but also the global flame-head morphology, the localized compression layer ahead of the recessed center, and the associated hydrodynamic redistribution. For hydrogen flames, low-Lewis-number transport and thermodiffusive instability may additionally influence local behavior; the present study is therefore framed as mechanism identification within a fixed LES closure rather than as a full transport-sensitivity assessment (Berger et al. 2025; Scalambro et al. 2025). Against this background, the paper pursues three objectives. It first identifies the three-dimensional, center-plane-dominant bifurcation mode selected by half-open confinement. It then organizes flame-head deformation, ahead-of-flame compression, tip-center velocity separation, and wake backflow within a single precursor framework. Finally, it examines whether changes in equivalence ratio primarily shift the entry timing and terminal strength of that pathway rather than alter

its underlying mechanism. The stoichiometric case ($\phi = 1.0$) was adopted as the reference condition, while the neighboring leaner and richer cases ($\phi = 0.9$ and 1.1) were used to examine how the same pathway is delayed or advanced with mixture strength.

2 Numerical Method and Case Setup

2.1 Geometry and boundary conditions

The computational domain was a plain rectangular channel, 0.24 m in length and 0.02 m $\times$ 0.02 m in cross-section. That simplicity was intentional. A more elaborate geometry would have mixed the confinement effect of interest here with obstacle-specific disturbances. By keeping the channel straight and unobstructed, the calculation forces the flame out of near-spherical growth soon after ignition and into a wall-controlled propagation mode. Rectangular hydrogen channels are commonly used for precisely this reason (Shen et al. 2021; Han et al. 2024).

The domain was half-open. Ignition was imposed at the closed left end, while the opposite end remained open for wave release. Pressure at the outlet used a wave-transmissive condition; velocity used pressureNormalInletOutletVelocity; temperature used an advective condition. The side walls were adiabatic and no-slip. This choice provides downstream relief without removing the localized compression layer that can still form ahead of a front whose streamwise advance is uneven (Wang et al. 2024a; Sheng et al. 2024; Wang et al. 2024b; Chu et al. 2025).

In that sense, the case lies between two simpler limiting pictures. It is not a sealed-duct deflagration, yet neither is it a fully open free expansion. What it creates instead is a one-sidedly confined channel in which branch-tip acceleration, centerline lag, ahead-of-flame compression, and wake backflow may all appear within the same stable propagation interval. Simplified wall-bounded hydrogen geometries are often adopted when the propagation sequence itself is the main object of study rather than the detailed reproduction of a specific engineering layout (Song et al. 2021; Shen et al. 2022).

2.2 Mesh, numerical solver, and combustion model

The computational grid was a structured hexahedral mesh with 320 $\times$ 30 $\times$ 30 cells in the streamwise, wall-normal, and spanwise directions. It was kept close to uniform on purpose. The intention was to avoid building an obvious grid preference into the later flame-head bifurcation, spanwise stratification, or localized compression signatures. The same mesh was retained for $\phi = 0.9$, 1.0, and 1.1 so that any inter-case difference would reflect mixture physics rather than a changed numerical representation.

To assess whether the bifurcated flame-head topology is tied to the reference mesh, an auxiliary mesh-resolution study was carried out for the baseline $\phi = 1.0$ case using three geometrically similar structured meshes (256 $\times$ 24 $\times$ 24, 320 $\times$ 30 $\times$ 30, and 384 $\times$ 36 $\times$ 36). Because the fine mesh develops earlier severe timestep restriction in the late stage, the comparison is restricted to the common stable interval t $\leq$ 0.620 ms. Within that interval, the same center-plane-dominant split-front topology, the same finite near-center spanwise extent of the bifurcated head, and the same qualitative

growth trend of D_b and $\Delta p_{\mathrm{ahead}}$ are recovered (Online Resource 2, Fig. S12–S15 and Table S5).

All simulations were run with rhoReactingFoam in LES mode. Subgrid stresses were modeled with WALE, and combustion was represented by the partially stirred reactor formulation with $C_{\mathrm{mix}} = 0.05$. Chemistry integration relied on the ODE solver, whereas thermophysical closure followed heRhoThermo + reactingMixture + janaf + perfectGas + sensibleEnthalpy. The chemical mechanism was a reduced H_2/O_2/air set with 10 species (H_2, H, O_2, O, OH, HO_2, H_2O_2, H_2O, AR, and N_2) and 27 reactions, converted from a Chemkin-type source into OpenFOAM format. Most converted entries retain the tag MARINOV 1995A, whereas the duplicated OH + HO_2 -> H_2O + O_2 channels retain HIPPLER 1995. Although automated adaptive chemistry strategies are increasingly available for LES of reacting flows (Amaduzzi et al. 2024), the present study uses the same reduced mechanism in all cases so that the inter-case comparison remains tied to mixture strength rather than case-specific chemistry adaptation.

The initial mixture states contain H_2, O_2, and N_2; AR remains only as an inert listed species and is not treated as an independent control parameter. Species transport and thermophysical properties follow the standard OpenFOAM Sutherland formulation together with the thermo package above. No separate multicomponent transport database was introduced, and no explicit Soret or related thermal-diffusion term was activated. These settings define the common numerical closure used in all three cases. They are not intended as case-by-case transport tuning; rather, they provide a fixed transport background against which the confinement-organized precursor pathway is identified. The associated interpretation limits for hydrogen-flame transport sensitivity are discussed in Section 5.4.

Time advancement used first-order Euler. Pressure-velocity coupling was handled with PIMPLE using nOuterCorrectors/nCorrectors/nNonOrthogonalCorrectors = 4/3/1, and maxCo was capped at 0.01 throughout. Those conservative settings were chosen because the analysis focuses on the ordered appearance of geometric, compressive, and hydrodynamic indicators over the usable propagation interval, not on an isolated local maximum. Numerical adequacy is therefore judged here by whether the precursor sequence and the associated cross-plane morphology are recovered consistently. Near termination, each run exhibited a sharp reduction in the adaptive time step. The interpretation of that late-stage numerical response is deferred to Section 5.3.

2.3 Initial conditions and ignition kernel

Before ignition, the channel was filled with quiescent premixed hydrogen-air at 1 atm and 293 K, and the velocity field was zero everywhere. The stoichiometric mixture ($\phi = 1.0$) served as the reference case. Two neighboring mixtures, $\phi = 0.9$ and $\phi = 1.1$, were introduced to test how a modest change in mixture strength shifts the same precursor pathway. Because the unburned mixture was not preheated, the high-temperature regions and compression signatures discussed below arise from ignition and subsequent confined propagation rather than from an imposed thermal bias.

Ignition was initiated near the closed end by a two-layer hot kernel centered at (0.009, 0.010, 0.010) m. The inner sphere had radius 0.0018 m and temperature 1000

K; it was surrounded by an outer layer of radius 0.0035 m at 550 K. The kernel is strong enough to ensure reliable ignition, yet compact enough for the ensuing flame development to remain governed by confinement rather than by an oversized imposed hot region.

2.4 Cases considered and definition of precursor quantities

Figure 1 summarizes the computational setup and the post-processing definitions used throughout the paper. Panel (a) shows the half-open geometry and boundary conditions. Panel (b) shows the structured mesh together with the two-layer ignition kernel. Panel (c) identifies the sampled z-planes and the center-plane quantities used later in the analysis.

Three mixtures were considered: $\phi = 0.9$, 1.0, and 1.1. The stoichiometric case was used to construct the precursor picture, whereas the leaner and richer mixtures were used to test how the same sequence shifts in timing and late-stage strength as mixture strength changes.

All precursor quantities were defined on the center plane z = 0.010 m and on the associated centerline y = 0.010 m, z = 0.010 m, where the flame-head split and its pressure-velocity signature are most clearly expressed. On that plane, the flame front was represented by the T = 1200 K contour. Its leading streamwise position is denoted x_{tip}, whereas its most recessed point is denoted x_{center}. The bifurcation depth is then $D_b = x_{\mathrm{tip}} - x_{\mathrm{center}}$.

For the compression metric, the centerline pressure was referenced to $p_0 = 101325$ Pa and reported as overpressure (p - p_0)/1000 in kPa. The ahead window was fixed at [x_{center}, x_{center} + 10 mm], and $\Delta p_{\mathrm{ahead}}$ was defined as the maximum overpressure within that interval. In practice, this window samples the compression layer immediately upstream of the recessed center-front region in a consistent manner across all three mixtures.

All cases were post-processed with identical definitions and the same extraction workflow. The comparison therefore isolates mixture-strength effects rather than changes in measurement procedure. The onset thresholds introduced below are operational timing markers for the present dataset, not universal critical values. Checks using neighboring front levels and modest variations of the ahead and wake windows preserved the inter-case ordering of the principal onset markers; for that reason, the reference definitions are retained in the main text.

3 Baseline Case: $\phi = 1.0$

The $\phi = 1.0$ case was used to establish the coupled precursor pathway because it provided the clearest combination of three-dimensional flame-head bifurcation, ahead-of-flame compression, and hydrodynamic redistribution while still retaining a usable stable propagation window. This section first documents the stratified flame morphology, then quantifies the geometric and compressive measures, and finally relates them to the evolving velocity field.

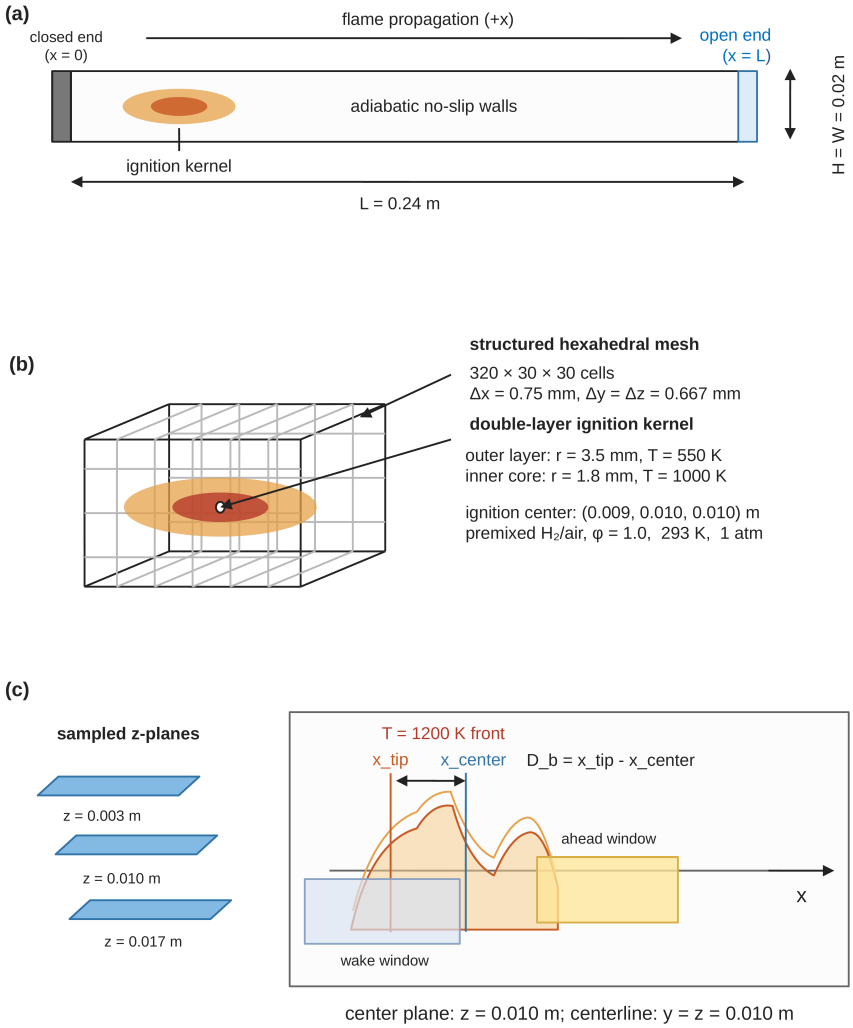


Fig. 1 Schematic summary of the LES configuration and post-processing definitions. (a) Half-open channel geometry and boundary conditions (L = 0.24 m, H = W = 0.02 m). (b) Structured 320 × 30 × 30 hexahedral mesh with the two-layer ignition kernel centered at (0.009, 0.010, 0.010) m; inner core r = 1.8 mm at T = 1000 K, outer layer r = 3.5 mm at T = 550 K. (c) Sampled z-planes and center-plane quantities used in post-processing, including the T = 1200 K front for x_{tip} and x_{center}, the bifurcation depth $D_b = x_{\mathrm{tip}} - x_{\mathrm{center}}$, the ahead-of-flame window $[x_{\mathrm{center}}, x_{\mathrm{center}} + 10\ \mathrm{mm}]$, and the wake-backflow window $[\max(0, x_{\mathrm{center}} - 20\ \mathrm{mm}), x_{\mathrm{center}}]$.

3.1 Morphological evidence of a confinement-induced three-dimensional bifurcated mode

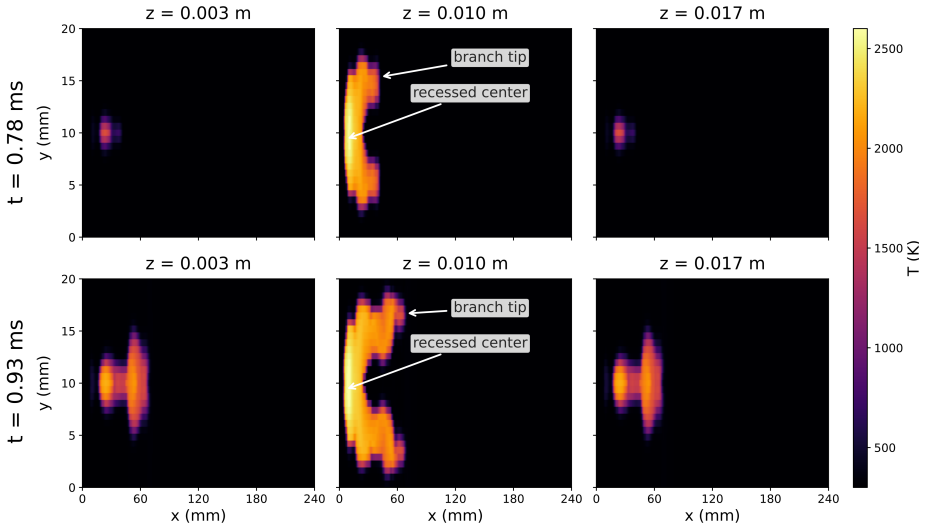


Fig. 2 Temperature slices at three spanwise locations (z = 0.003, 0.010, and 0.017 m) for the baseline case with $\phi = 1.0$ at t = 0.78 ms and t = 0.93 ms. The center plane develops the clearest double-branch flame head, whereas the off-center planes remain comparatively narrower and less bifurcated, demonstrating that the bifurcated flame head is a genuinely three-dimensional stratified feature

Figure 2 presents temperature slices at z = 0.003, 0.010, and 0.017 m at t = 0.78 and 0.93 ms. Once confinement becomes dominant after the early kernel-expansion stage, the front no longer retains an approximately spherical form. Instead, it adopts a spanwise-stratified propagation mode in which the center plane exhibits the clearest double-branch flame head, whereas the off-center planes remain narrower and less bifurcated. The bifurcation is therefore a genuinely three-dimensional feature rather than an artifact of a single slice.

As the flame advances, the central portion of the front falls progressively behind the side branches, producing a recessed centerline region. This asynchronous advance provides the visible signature of wall-constrained differential propagation.

Figure 3 presents the corresponding streamwise velocity field. Local acceleration is strongest near the bifurcated branch tips, whereas the recessed center region remains comparatively slow. The geometrically leading portions of the front are thus also dynamically favored, and the tip-center velocity contrast emerges naturally as a precursor metric.

Together, Figs. 2 and 3 show that the baseline flame evolves into a three-dimensional bifurcated structure characterized by spanwise stratification and non-uniform streamwise acceleration across the flame head. In broad physical terms, this behavior is consistent with previous studies of confined hydrogen flames and no-slip-wall flame dynamics, which likewise report pronounced flame deformation and

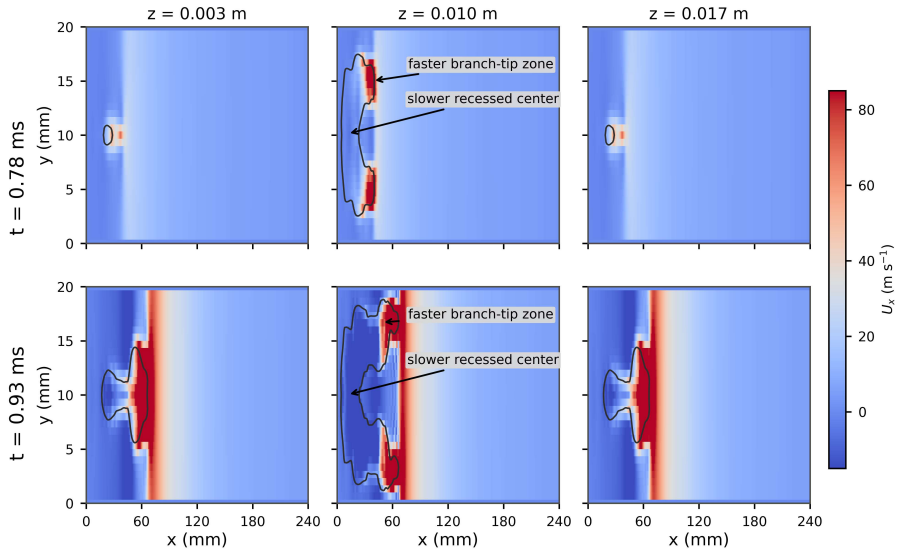


Fig. 3 Streamwise-velocity slices at three spanwise locations (z = 0.003, 0.010, and 0.017 m) for the baseline case with $\phi = 1.0$ at t = 0.78 ms and t = 0.93 ms. Strong local acceleration develops near the branch tips, while the recessed center region remains relatively slower, linking the evolving flame morphology to the growth of tip-center velocity separation

flow-field reorganization under confinement (Shen et al. 2023; Liberman et al. 2023; Han et al. 2024; Shen et al. 2025; Xia et al. 2026).

3.2 Quantification of recessed-center recession and branch-tip dominance

Figure 4 quantifies the separation between the advancing branch tips and the recessed center. At early times, x_{tip} and x_{center} remain close. Later, the branch tips continue to advance while the center lags behind, rapidly opening the flame head.

The same trend is compactly captured by the formal bifurcation depth D_b. In the baseline case, D_b remains small initially and then rises sharply, marking the transition from a relatively compact front to a clearly branch-dominated structure.

D_b thus converts the visual bifurcation seen in Fig. 2 into a directly traceable geometric precursor and provides a natural link between flame-head deformation and the altered loading of the unburned gas ahead of the front.

3.3 Ahead-of-flame compression buildup and coupled mechanism trajectory

Figure 5 shows that ahead-of-flame compression stays weak at first and then rises rapidly once the flame head becomes unmistakably bifurcated. A localized compression layer is thereby established immediately upstream of the recessed portion of the front.

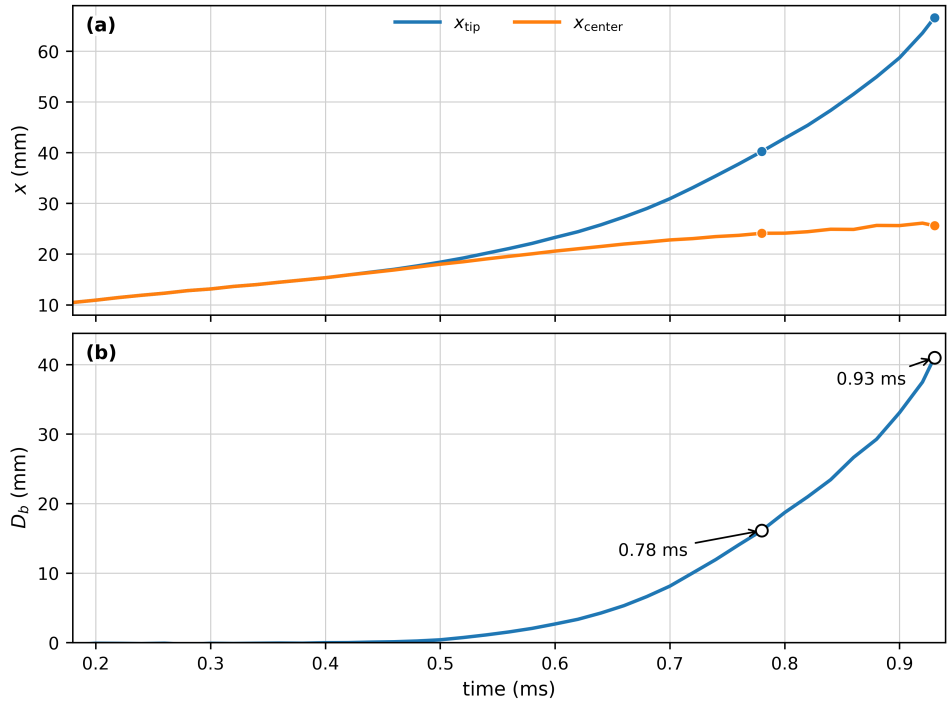


Fig. 4 Evolution of branch-tip advance and recessed-center recession for the baseline case ($\phi = 1.0$). Panel (a) compares the leading flame-tip position x_{tip} and the recessed center position x_{center} on the center-plane T = 1200 K contour, while panel (b) shows the resulting formal bifurcation depth $D_b = x_{\mathrm{tip}} - x_{\mathrm{center}}$

That point matters because the configuration is half-open rather than fully closed. Outlet relief restrains uniform global pressurization, yet it does not eliminate the local compression generated by a front whose streamwise advance is uneven.

Figure 6 makes the coupling easier to read by tracing the evolution in the (D_b, $\Delta p_{\mathrm{ahead}}$) plane. The trajectory leaves a weakly deformed, weakly compressed state and turns toward a late-stage branch on which structural amplification and local compression strengthen together.

The baseline flame therefore approaches its strongest stable state through coupled structural-compressive growth, not through an isolated geometric change or a solely pressure-driven response. Earlier confined and vented hydrogen studies were not framed in this precursor language, but they remain broadly compatible with the physical picture obtained here (Jiang et al. 2024a; Jiang et al. 2024b; Cao et al. 2024; Chu et al. 2025; Qu et al. 2025).

3.4 Hydrodynamic redistribution and integrated precursor framework

The structural and compressive amplification documented above is accompanied by a marked reorganization of the flow field. As the bifurcation deepens, streamwise motion

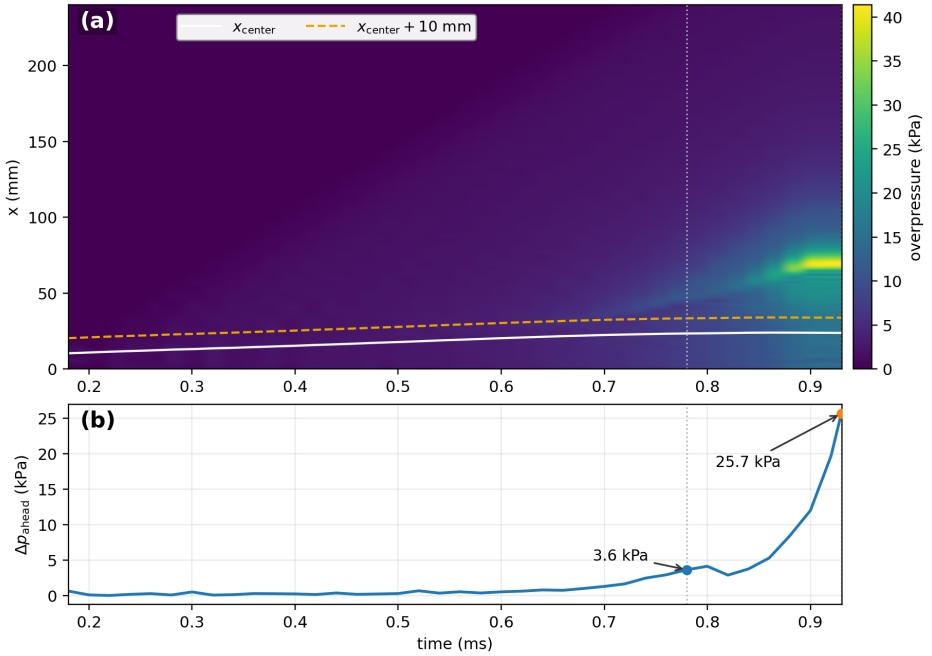


Fig. 5 Ahead-of-flame compression for the baseline case ($\phi = 1.0$). $\Delta p_{\mathrm{ahead}}$ is evaluated along the centerline over $[x_{\mathrm{center}}, x_{\mathrm{center}} + 10\ \mathrm{mm}]$. The pressure rise remains modest at early times and grows rapidly as the coupled flame structure develops.

near the leading branch tips separates progressively from that in the recessed center region.

This separation is quantified by the tip-center velocity difference $\Delta U = U_{\mathrm{tip}}$ - U_{center} in Fig. 7(a). In the baseline case, ΔU rises from about 6.9 m s^{-1} at t = 0.78 ms to about 49.0 m s^{-1} at t = 0.93 ms, indicating a marked late-stage strengthening of branch-tip dominance.

A similarly clear change appears in the wake behind the recessed center. Along the centerline, the minimum streamwise velocity within [max(0, x_{center} - 20 mm), x_{center}] becomes increasingly negative as the flame advances. In the baseline case, U_{back} decreases from about -5.0 m s^{-1} at t = 0.78 ms to about -22.4 m s^{-1} at t = 0.93 ms, indicating the growth of an organized recirculating wake.

The velocity-based indicators reinforce the same interpretation provided by D_b and $\Delta p_{\mathrm{ahead}}$: as the flame develops, bifurcation intensifies, compression loading ahead of the front increases, and the wake behind the recessed center becomes more organized.

A late-stage numerical deterioration is also observed near termination. Because that response concerns terminal solver behavior rather than the precursor pathway itself, it is discussed separately in Section 5.3.

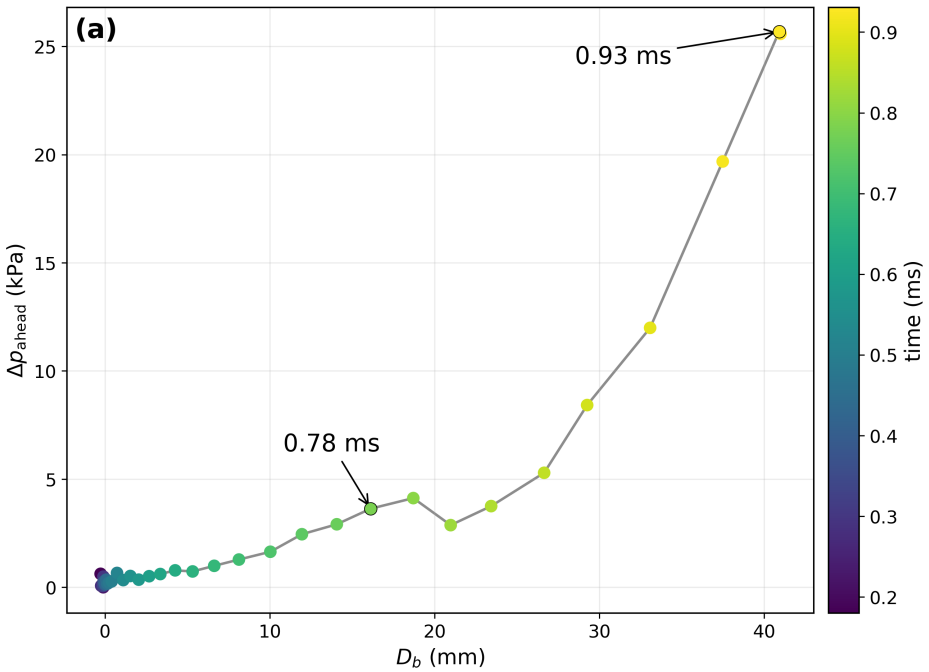


Fig. 6 Trajectory of the baseline case ($\phi = 1.0$) in the (D_b, $\Delta p_{\mathrm{ahead}}$) plane. Structural bifurcation growth and ahead-of-flame compression intensify concurrently, leading to the strongest stable coupled state.

4 Effect of Equivalence Ratio

With the baseline pathway established, the remaining question is how that same sequence responds to modest departures from stoichiometric conditions. Across this comparison, geometry, ignition configuration, boundary conditions, solver settings, and combustion-model parameters were held fixed; equivalence ratio was the only deliberate physical control variable. The differences seen below can therefore be interpreted as mixture-strength effects rather than as consequences of a changed numerical or geometric framework.

4.1 Event sequence under different equivalence ratios

Figure 8 compresses the inter-case comparison into three time markers: the first occurrence of $D_b \geq 5$ mm, the first occurrence of $\Delta p_{\mathrm{ahead}} \geq 3$ kPa, and the last stable output time. Even in that reduced view, the ordering is clear. The richer mixture reaches the coupled regime first, the leaner mixture last, and the stoichiometric case remains between them.

In the $\phi = 1.1$ case, both onset criteria are crossed first, so the structurally amplified and locally compressed state is entered earliest there. At the opposite end, $\phi = 0.9$

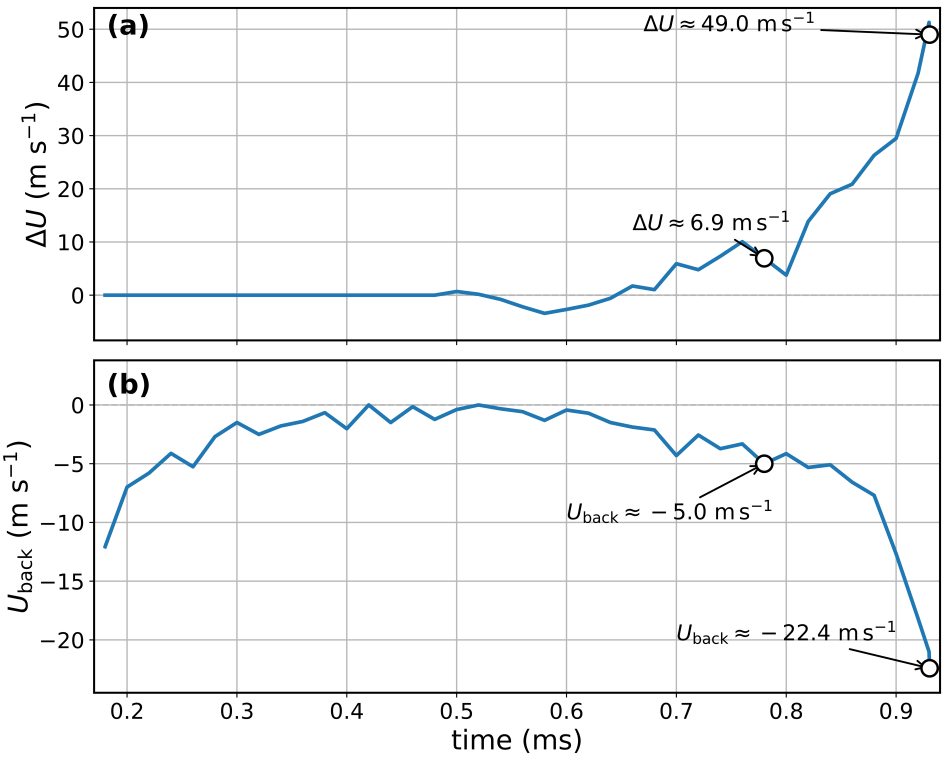


Fig. 7 Hydrodynamic precursor evolution for the baseline case ($\phi = 1.0$). Panel (a) reports the tip-center streamwise-velocity difference $\Delta U = U_{\mathrm{tip}}$ - U_{center}, where U_{tip} is sampled at the two leading branch-tip positions on the center-plane T = 1200 K front and U_{center} is the centerline Ux value at x = x_{center}. Panel (b) reports the wake-backflow metric U_{back} extracted over [max(0, x_{center} - 20 mm), x_{center}]. The late propagation stage is characterized by strong hydrodynamic non-uniformity and an intensified negative wake behind the recessed center.

reaches the same criteria last and therefore spends a larger portion of its stable window in a comparatively weakly developed regime. The stoichiometric mixture again occupies an intermediate position.

What changes with ϕ is not the sequence itself, but the time along the evolution at which that sequence becomes pronounced.

That ordering is not an artifact of a single definition. Replacing the center-plane front by T = 1100, 1200, or 1300 K leaves the onset order of the $D_b \geq 5$ mm marker unchanged. Changing the ahead window from 8 to 12 mm leaves the onset order of the $\Delta p_{\mathrm{ahead}} \geq 3$ kPa marker unchanged as well. These checks are reported in Online Resource 1 (Fig. S7, Fig. S8, and Table S1). The forward shift with increasing ϕ should therefore be read as a robust inter-case trend within the present dataset, rather than as a by-product of the reference definitions used in the main text.

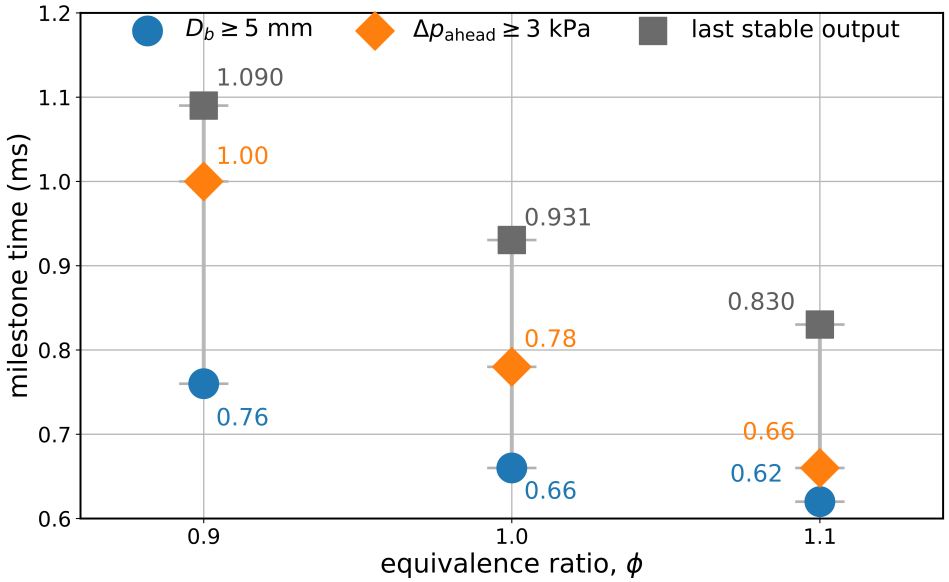


Fig. 8 Timing comparison for $\phi = 0.9$, 1.0, and 1.1. For each case, three milestones are reported: the first occurrence of $D_b \geq 5$ mm, the first occurrence of $\Delta p_{\text{ahead}} \geq 3$ kPa, and the last stable output time. Increasing ϕ displaces the same coupled precursor sequence toward earlier times.

4.2 Comparison of structural, compressive, and coupled precursor growth

Figure 9 resolves the same comparison in more detail. Panel (a) shows $D_b(t)$, panel (b) shows $\Delta p_{\text{ahead}}(t)$, and panel (c) combines both measures in the (D_b, Δp_{ahead}) plane.

The first clear departure from the weak-bifurcation regime occurs in the $\phi = 1.1$ case. In other words, branch-tip dominance and center recession set in earliest for the richer mixture. The $\phi = 0.9$ case remains longest near the low-D_b state, while the stoichiometric case falls between those two limits.

The pressure metric follows the same order. In the richer case, an appreciable local overpressure appears earlier; in the leaner case, Δp_{ahead} stays weaker through much of the usable propagation interval. Structural deformation and local compression therefore advance in step as ϕ increases.

Panel (c) gives the clearest inter-case summary. All three mixtures move along the same qualitative route—from a weakly deformed, weakly compressed state toward a more strongly coupled one. The differences lie in how early each case enters that route and in how far it proceeds before stable forward propagation is lost. The richer mixture enters first, the stoichiometric case attains the strongest stable terminal state, and the leaner case follows the same route more gradually.

Taken together, the results support a common mechanism rather than different terminal classes. Figure 10 pushes the comparison one step further by evaluating D_b and Δp_{ahead} at matched normalized stages, $\tau \approx 0.70$, 0.80, and 0.90.

Normalization does not collapse the three cases onto a single curve. By the late normalized stage, the stoichiometric mixture still carries the strongest structural

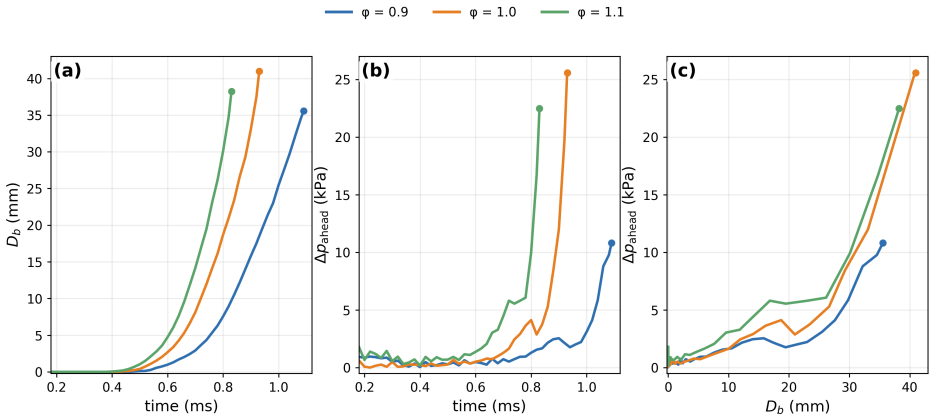


Fig. 9 Absolute-time development of the precursor quantities at different equivalence ratios. (a) D_b(t). (b) $\Delta p_{\mathrm{ahead}}$(t). (c) Corresponding trajectories in the (D_b, $\Delta p_{\mathrm{ahead}}$) plane. The richer mixture enters the coupled regime first, whereas the stoichiometric case reaches the strongest stable terminal state.

and compressive amplification, whereas the richer case, despite its earlier absolute-time development, no longer leads both metrics. Equivalence ratio therefore governs not only when the pathway is entered, but also how strongly structural-compressive coupling develops within the remaining stable portion of the window.

This normalized-stage separation shows that earlier entry into the coupled regime does not automatically imply the strongest late-stage coupled state. A plausible interpretation is that equivalence ratio controls both the onset timing of structural-compressive amplification and the remaining interval over which that amplification can continue before stable forward propagation is lost. In the present dataset, the richer mixture advances the onset of bifurcation and compression, whereas the stoichiometric mixture sustains stronger amplification deeper into the stable window; correspondingly, at $\tau \approx 0.90$, the $\phi = 1.0$ case still exceeds $\phi = 1.1$ in both D_b and $\Delta p_{\mathrm{ahead}}$ (Online Resource 1, Table S3). The role of equivalence ratio is therefore not reducible to a simple monotonic acceleration of the same response; it also affects how the available stable interval is distributed between early entry and late-stage strengthening.

Additional hydrodynamic comparisons are provided in Online Resource 1. Figure S5 shows that ΔU and the negative wake response strengthen earlier in the richer and stoichiometric cases than in the leaner one, while Fig. S6 compares the terminal values of D_b, $\Delta p_{\mathrm{ahead}}$, ΔU, and U_{back} across all three mixtures. Together with the normalized-stage support in Fig. S10 and Fig. S11, these supplementary results support the same interpretation: velocity redistribution develops alongside D_b and $\Delta p_{\mathrm{ahead}}$ as part of the same coupled pathway, not as a separate mechanism class.

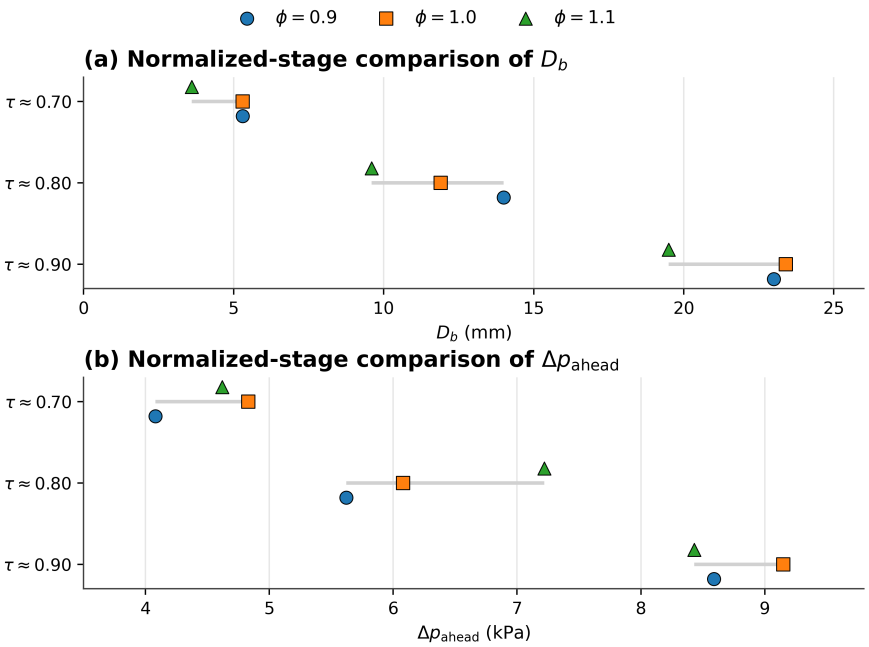


Fig. 10 Comparison at matched normalized stages for different equivalence ratios. (a) D_b at $\tau \approx 0.70$, 0.80, and 0.90. Each horizontal gray segment denotes the span across the three cases at a given stage. (b) Corresponding values of $\Delta p_{\mathrm{ahead}}$ evaluated with the reference ahead window $[x_{\mathrm{center}}, x_{\mathrm{center}} + 10$ mm] and $p_0 = 101325$ Pa. The cases remain separated after normalization, and the stoichiometric mixture retains the strongest late-stage structural-compressive state.

5 Discussion

Overall, the foregoing results show that half-open confinement does more than restrict expansion; it also orders the emergence of deformation, compression, and flow redistribution. The discussion therefore focuses on four questions: why the bifurcation is clearest on the center plane, why local compression remains significant despite outlet relief, how the late-stage numerical deterioration should be interpreted within the present dataset, and how the omission of explicit multicomponent thermal-diffusion effects bounds the physical interpretation.

5.1 Center-plane bifurcation under half-open confinement

Half-open confinement does more than restrict flame growth; it selects a distinct mode of front evolution. Once wall effects dominate the early kernel-expansion stage, downstream advance proceeds under asymmetric confinement and the front reorganizes into a recessed center flanked by two laterally favored branches. The observed bifurcation is therefore a system-level response to confinement rather than a local irregularity of an otherwise compact front. This interpretation is consistent with classical studies of finger-flame acceleration and no-slip-wall effects in tubes (Akkerman et al. 2006; Bychkov et al. 2007).

This picture also complements recent flame-wall-interaction studies that emphasize wall-induced flow deceleration and transport reorganization near solid boundaries (Ahmed et al. 2023; Ahmed et al. 2024). In the present half-open channel, those wall effects do not remain localized. Rather, their spanwise accumulation is expressed most symmetrically on the center plane, where the competing lateral branches separate most clearly and the recessed-center lag becomes most pronounced. The center-plane bifurcation identified here should therefore be read as a channel-scale three-dimensional manifestation of wall-confinement effects, not merely as a local contour deformation.

The center plane is the location at which this branch competition is expressed most symmetrically, and it is therefore where the split front appears most clearly. Off-center planes remain more strongly influenced by one-sided wall proximity and accordingly stay narrower and less fully separated. The center-plane-dominant bifurcation should thus be interpreted as a channel-scale three-dimensional propagation mode rather than as a contour artifact.

This interpretation is supported by the supplementary mesh study of the baseline ϕ = 1.0 case. Within the common stable interval, the coarse, baseline, and fine meshes all recover the split-front topology on the center plane, and a near-center off-plane section (z = 0.013 m) likewise exhibits a resolved split front, whereas the farther off-center sections do not yet show a comparably resolved split T = 1200 K contour (Online Resource 2, Fig. S12 and Fig. S15). The spanwise pattern is therefore better read as a finite three-dimensional extent of the bifurcated head than as a directional-grid or single-section artifact.

The growth of D_b supports the same reading: once the branch tips advance more efficiently than the center region, the front becomes branch-dominated rather than compact. Stratification, centerline recession, and flame-head bifurcation are therefore different manifestations of the same confinement-organized response.

5.2 Why local compression remains strong despite outlet relief

Outlet relief does not eliminate local compression. Rather, it prevents the event from becoming purely globally pressurized while still allowing a flame-ahead compression layer to develop locally. The half-open configuration therefore separates partial global pressure relief from local compressive loading immediately ahead of the flame.

Experiments and simulations of vented and semi-open hydrogen systems similarly show that pressure relief and local compression can coexist (Wang et al. 2024a; Sheng et al. 2024; Wang et al. 2024b; Chu et al. 2025). In the present case, outlet relief limits global accumulation but does not prevent the bifurcated front from driving non-uniform displacement and compression of the unburned gas upstream.

Once the flame head becomes strongly bifurcated, the gas ahead of the front is no longer loaded uniformly. The trajectory in the (D_b, $\Delta p_{\mathrm{ahead}}$) plane shows that geometric deformation and local compression intensify together. A plausible interpretation is that the recessed center and the advancing branch tips reorganize the local flow such that compressive loading becomes concentrated within the centerline ahead window used here.

The hydrodynamic indicators support the same interpretation: ΔU captures growing branch-tip dominance, and U_{back} records the increasingly organized recirculation

behind the recessed center. The compression layer is therefore one element of the same confinement-induced coupled pathway rather than an unrelated pressure event.

5.3 Why the terminal solver difficulty is more plausibly associated with localized stiffening

The numerical deterioration observed near the end of the stable propagation window is best interpreted against the background of the underlying physical amplification. As the coupled state intensifies, the adaptive time step collapses rapidly while $Co_{\max}$ remains comparatively bounded. If the terminal behavior were controlled primarily by a conventional global Courant-number limit, a more pronounced increase in $Co_{\max}$ would ordinarily be expected.

The late-stage numerical response is therefore not taken as evidence of a single resolved source region. Rather, it is interpreted as a secondary manifestation of the strongly coupled late-stage state, in which steep temperature, species, pressure, and velocity gradients coexist with the most strongly deformed flame structure. Within the limits of the present dataset, this pattern is more consistent with localized stiffening than with a predominantly global CFL excursion, although the precise spatial origin of that stiffness remains unresolved.

The term numerical lock-up is used here in a restricted practical sense. It denotes the loss of stable forward advancement, not a claim that the late-stage dynamics are merely numerical artifacts. The central result of the study remains the identification of an ordered confinement-organized precursor pathway linking flame-head bifurcation, local compression loading, branch-tip dominance, and wake backflow.

Recent studies of hydrogen channels and vented deflagrations likewise indicate that mixture strength or hydrogen concentration can shift the onset of intensified flame deformation and pressure response (Cao et al. 2024; Qu et al. 2025; Wang et al. 2025). The present results extend that picture by showing that, in a three-dimensional half-open channel, ϕ primarily advances or delays entry into the same precursor pathway rather than producing distinct terminal mechanisms.

5.4 Possible role of thermodiffusive instability under the present closure

The present LES framework deliberately uses a common transport closure without explicit multicomponent diffusion or Soret terms, because the central objective of this study is to isolate the confinement-organized morphology-compression-hydrodynamics sequence under fixed numerical and physical settings. In other words, the paper is designed to identify a wall-confinement-induced precursor pathway, not to exhaust the full transport sensitivity of hydrogen flames. The conclusions reported above should therefore be read first as mechanism-identification and inter-case-ordering statements under a common closure.

For hydrogen-air flames, however, low-Lewis-number transport, stretch-sensitive modelling, advanced diffusion treatment, and thermodiffusive instability can modify local flame wrinkling, cellularity, and curvature-sensitive burning response (Berger et al. 2025; Mehl et al. 2024; Haider et al. 2025; Scalambro et al. 2025). Within the narrow

equivalence-ratio range considered here, such effects are expected to be more relevant on the lean side than on the rich side. A reasonable implication for the present problem is that omitted thermodiffusive transport could quantitatively alter the onset timing or magnitude of the precursor indicators, especially where flame-head curvature, local stretch, and near-wall confinement act simultaneously.

This does not overturn the pathway identified in Sections 3-4. Rather, it places a bound on how the present results should be interpreted: thermodiffusive instability may modulate the local expression of the confinement-induced pathway, but it is not introduced here as a separate mechanism class. Future work should extend the present framework by incorporating multicomponent transport and explicit thermal-diffusion treatment to examine how low-Lewis-number effects interact with wall-confinement-induced bifurcation, ahead-of-flame compression, and wake reorganization.

5.5 Scope and limitations

The present study is deliberately framed as mechanism identification within a fixed numerical framework. It is not intended to establish universal thresholds for bifurcation or compression, nor to replace a broader program of mesh, model, and parameter-robustness analysis. Rather, the objective is to isolate the ordered morphology-compression-hydrodynamics sequence generated by half-open confinement under one internally consistent LES setup.

The supplementary material provides internal-consistency support through neighboring front definitions, variations in the ahead and wake windows, threshold sensitivity, normalized-stage comparisons, and an auxiliary mesh-resolution study for the baseline case within a common stable interval. The latter is used to test topology/trend robustness rather than strict late-stage quantitative convergence: within $t \leq 0.620$ ms, the coarse, baseline, and fine meshes recover the same center-plane-dominant bifurcation topology and the same qualitative growth trend of D_b and $\Delta p_{\mathrm{ahead}}$, while the absolute metric values at matched times remain mesh-sensitive (Online Resource 2, Table S5). Even so, the thresholds adopted here remain operational comparison markers for the present dataset rather than universal critical values. The present results should therefore not be transferred directly to other channel sizes, outlet conditions, ignition layouts, chemistry/transport assumptions, or closure settings without further verification. The principal value of the present framework lies in mechanistic clarity and inter-case ordering within a fixed configuration, rather than in broad parametric generalization.

6 Conclusions

The principal conclusions of the present LES study of three-dimensional premixed hydrogen-air flame propagation in a half-open channel can be stated as follows.

1. Half-open confinement suppresses prolonged quasi-spherical expansion and reorganizes the flame into a three-dimensional stratified mode, with the center plane displaying the clearest flame-head bifurcation and recessed-center lag.

2. Flame-head bifurcation, ahead-of-flame compression, tip-center velocity separation, and wake backflow develop as coupled precursors rather than as disconnected late-stage observations.
3. The same coupled pathway is recovered for $\phi = 0.9$, $\phi = 1.0$, and $\phi = 1.1$. The richer mixture enters the pathway earliest and the leaner mixture latest in absolute time; this ordering remains unchanged under neighboring front definitions and modest variations of the ahead and wake windows. Earlier entry, however, does not imply the strongest normalized late-stage coupled state: at matched normalized stages, the stoichiometric case retains the strongest late-stage structural-compressive amplification within the stable propagation window.
4. Near termination, the adaptive time step collapses sharply while $Co_{\max}$ remains comparatively controlled. Within the limits of the present dataset, this response is treated as a secondary late-stage manifestation accompanying the strongly coupled state rather than as the central physical result of the study.
5. A supplementary mesh-resolution study for the baseline $\phi = 1.0$ case shows that, within the common stable interval $t \leq 0.620$ ms, the center-plane split-front topology, its finite near-center spanwise extent, and the qualitative growth trend of D_b and $\Delta p_{\mathrm{ahead}}$ are all recovered on systematically refined structured meshes. The mesh evidence therefore supports topology/trend robustness and argues against a directional-grid interpretation of the bifurcation.

Overall, the precursor framework developed here provides a compact, mechanism-oriented basis for future robustness studies addressing mesh resolution, model choice, chemistry/transport treatment, and broader variation in mixture conditions in half-open hydrogen-air channels.

Supplementary information. Online Resource 1 (ESM_1.pdf) contains the supplementary slices, inter-case hydrodynamic comparisons, robustness checks, and normalized-stage support data used in the main text. Specifically, Fig. S1-S4 provide supplementary temperature and velocity slices for $\phi = 0.9$ and $\phi = 1.1$; Fig. S5-S6 provide inter-case hydrodynamic and terminal-support comparisons; Fig. S7-S11 document front-definition robustness, ahead-window sensitivity, wake-window sensitivity, and normalized-stage comparisons; and Table S1-S4 summarize onset robustness, threshold sensitivity, normalized-stage values, and representative-time support values.

Online Resource 2 (ESM_2.pdf) contains the supplementary mesh-resolution study for the baseline $\phi = 1.0$ case. Fig. S12–S15 compare center-plane contour topology, centerline overpressure profiles, precursor-metric evolution, and spanwise contour overlays on coarse, baseline, and fine meshes within the common stable interval $t \leq 0.620$ ms, and Table S5 summarizes the matched-time mesh-comparison values.

Declarations

Funding

This work was supported by the 2025 Undergraduate Innovation and Entrepreneurship Training Program of Inner Mongolia Autonomous Region, China (Grant No. S202510128025).

Author contributions

Youquan Yuan developed the computational workflow, ran the simulations and post-processing, prepared the figures, and drafted the manuscript. Jiandong He supervised the study, provided resources and funding support, and revised the manuscript critically.

Competing interests

The authors report no financial, professional, or personal conflicts that are relevant to this study.

Data availability

The processed datasets underlying Figs. 4–10, together with the CSV files used for the main-text plots and the supplementary slice and line-extraction data used to assemble the supporting figures, can be obtained from the corresponding author on reasonable request. The reconstructed raw OpenFOAM case files are substantially larger and can likewise be shared for research purposes, subject to practical file-transfer limits.

Code availability

The scripts used for post-processing and figure generation can be obtained from the corresponding author on reasonable request. They include the ParaView/Python extraction routines, the CSV assembly utilities, and the plotting scripts used to generate the main-text figures and the associated robustness checks.

References

[1] Ahmed, U., Chakraborty, N., Klein, M.: Influence of Flow Configuration and Thermal Wall Boundary Conditions on Turbulence During Premixed Flame-Wall Interaction within Low Reynolds Number Boundary Layers. Flow Turbul. Combust. 111, 825–866 (2023). https://doi.org/10.1007/s10494-023-00437-y.

[2] Ahmed, U., Ghai, S.K., Chakraborty, N.: Assessment of Laws of the Wall During Flame–Wall Interaction of Premixed Flames Within Turbulent Boundary Layers. Flow Turbul. Combust. 112, 1161–1190 (2024). https://doi.org/10.1007/s10494-024-00541-7.

[3] Akkerman, V., Bychkov, V., Petchenko, A., Eriksson, L.E.: Accelerating flames in cylindrical tubes with nonslip at the walls. Combust. Flame 145(1–2), 206–219 (2006). https://doi.org/10.1016/j.combustflame.2005.10.011.

[4] Amaduzzi, R., D'Alessio, G., Pagani, P., Cuoci, A., Malpica Galassi, R., Parente, A.: Automated adaptive chemistry for large eddy simulations of turbulent reacting flows. Combust. Flame 259, 113136 (2024). https://doi.org/10.1016/j.combustflame.2023.113136.

[5] Berger, L., Attili, A., Gauding, M., Pitsch, H.: LES combustion model for premixed turbulent hydrogen flames with thermodiffusive instabilities: a priori and a posteriori analysis. J. Fluid Mech. 1003, A33 (2025). https://doi.org/10.1017/jfm.2024.1201.

[6] Bychkov, V., Akkerman, V., Fru, G., Petchenko, A., Eriksson, L.E.: Flame acceleration in the early stages of burning in tubes. Combust. Flame 150(4), 263–276 (2007). https://doi.org/10.1016/j.combustflame.2007.01.004.

[7] Cao, Y., Sun, A., Hua, M., Pan, X.: Influence of hydrogen concentration on the pressure oscillation and flame propagation during vented deflagration of hydrogen-air mixtures. Int. J. Hydrogen Energy 64(97), 798–805 (2024). https://doi.org/10.1016/j.ijhydene.2024.03.347.

[8] Chu, Z., Chen, R., Li, X., Xu, Z., Shi, X., Cao, W., Fu, G., Xu, J., Zhou, W., Zhang, Y.: Characteristics of hydrogen-air premixed explosion venting in a cabinet vessel under different bursting pressures. Int. J. Hydrogen Energy 186, 151981 (2025). https://doi.org/10.1016/j.ijhydene.2025.151981.

[9] Haider, A., Morev, I., Rintanen, A., Shahin, Z., Tamadonfar, P., Karimkashi, S., Wehrfritz, A., Vuorinen, V.: Accelerated numerical simulations of hydrogen flames: open-source implementation of an advanced diffusion model library in OpenFOAM. Int. J. Hydrogen Energy 189, 152115 (2025). https://doi.org/10.1016/j.ijhydene.2025.152115.

[10] Han, H., Ma, Q., Qin, Z., Li, Y., Kong, Y.: Experimental study on combustion and explosion characteristics of hydrogen-air premixed gas in rectangular channels with large aspect ratio. Int. J. Hydrogen Energy 57, 1041–1050 (2024). https://doi.org/10.1016/j.ijhydene.2024.01.125.

[11] Jiang, Y., Qiu, S., Gao, W., Liang, B., Li, Y.: Hydrogen flame acceleration and explosion overpressure characteristics in a closed obstructed duct. Int. J. Hydrogen Energy 59, 1–9 (2024a). https://doi.org/10.1016/j.ijhydene.2024.01.291.

[12] Jiang, Y., Gao, W., Sun, Z., Liang, B., Zhang, K., Li, Y.: Experimental and numerical study on explosion behavior of hydrogen-air mixture in an obstructed closed chamber. Int. J. Hydrogen Energy 49(Pt A), 1032–1045 (2024b). https://doi.org/10.1016/j.ijhydene.2023.08.159.

[13] Liberman, M.A., Qian, C., Wang, C.: Dynamics of flames in tubes with no-slip walls and the mechanism of tulip flame formation. Combust. Sci. Technol. 195, 1637–1665 (2023). https://doi.org/10.1080/00102202.2023.2182204.

[14] Liu, Q., Xu, Z., Yang, G., Sun, H., Zhang, S.: Study on the explosion characteristics of premixed hydrogen-air mixtures in a wavy confined pipe. Process Saf. Environ. Prot. 208, 108538 (2026). https://doi.org/10.1016/j.psep.2026.108538.

[15] Mehl, C., Poncet, S., Truffin, K., Colin, O.: Large eddy simulation of large-scale hydrogen deflagrations using the thickened flame model with stretch sensitivity adaptation and thermo-diffusive instability modeling. Int. J. Hydrogen Energy 93(1–2), 457–468 (2024). https://doi.org/10.1016/j.ijhydene.2024.10.169.

[16] Ponizy, B., Claverie, A., Veyssière, B.: Tulip flame - the mechanism of flame front inversion. Combust. Flame 161(12), 3051–3062 (2014). https://doi.org/10.1016/j.combustflame.2014.06.001.

[17] Qian, C., Liberman, M.A.: On the mechanism of "tulip flame" formation: The effect of ignition sources. Phys. Fluids 35(11), 116122 (2023). https://doi.org/10.1063/5.0174234.

[18] Qu, J., Zhao, H., Zhao, L., Luo, Z.-M., Wang, T., Deng, J.: Flame propagation characteristics of non-uniform premixed hydrogen-air mixtures explosion in a pipeline. Int. J. Hydrogen Energy 88, 462–476 (2024). https://doi.org/10.1016/j.ijhydene.2024.09.235.

[19] Qu, J., Zhao, H., Wang, C., Luo, Z., Cheng, F., Wang, T., Li, H., Zhao, L., Zhou, T., Wang, R., Deng, J.: Coupled analysis between explosion overpressure and flame propagation characteristics of H_2-air premixed gas. Int. J. Hydrogen Energy 101, 568–581 (2025). https://doi.org/10.1016/j.ijhydene.2024.12.468.

[20] Scalambro, A., Piano, A., Millo, F.: Modelling thermodiffusive instabilities in hydrogen flames and their impact on the combustion process in a direct-injection hydrogen engine. Combust. Flame 282, 114457 (2025). https://doi.org/10.1016/j.combustflame.2025.114457.

[21] Shen, T., Li, M., Xiao, H.: Propagation of premixed hydrogen-air flame initiated by a planar ignition in a closed tube. Int. J. Hydrogen Energy 47(7), 4903–4915 (2022). https://doi.org/10.1016/j.ijhydene.2021.11.123.

[22] Shen, X., Xu, J., Wen, J.X., Wen, X.L.: Phenomenological characteristics of hydrogen-air premixed flame propagation in closed rectangular channels. Renew. Energy 174, 606–615 (2021). https://doi.org/10.1016/j.renene.2021.04.056.

[23] Shen, X., Shen, J., Liu, H., Wen, J.X., Ma, Y., Zou, X., Liu, Z.: Numerical investigation on dynamic behavior of premixed hydrogen-air flame propagation in a closed tube. Fuel 354, 129295 (2023). https://doi.org/10.1016/j.fuel.2023.129295.

[24] Shen, X., Wang, W., Ma, Y., Wen, J.X., Wen, X.L.: Flame dynamics, three-dimensional structure and flow field of premixed H_2-air flame with heat loss. Renew. Energy 245, 122805 (2025). https://doi.org/10.1016/j.renene.2025.122805.

[25] Sheng, Y., Luo, Z., Liu, L., Yang, Z., Meng, F., Dong, Z., Zhang, Y., Qu, J., Deng, J., Wang, T.: Experimental investigation on the vented flame and pressure

behaviour of hydrogen-air mixtures. J. Loss Prev. Process Ind. 92, 105469 (2024). https://doi.org/10.1016/j.jlp.2024.105469.

[26] Song, Y., Zhang, Y., Chen, Y., Liu, X., Fu, M., Li, Y.: Numerical investigation of effects on premixed hydrogen-air flame propagation in a pipe with different contraction or expansion angles. J. Loss Prev. Process Ind. 70, 104201 (2021). https://doi.org/10.1016/j.jlp.2020.104201.

[27] Wang, F., Huang, S., Xu, C., Wang, C., Guo, J., Lin, J.: Experimental and numerical study on vented H_2-air explosion in an obstructed duct: effects of hydrogen concentration and vent size. Int. J. Hydrogen Energy 143, 330–339 (2025). https://doi.org/10.1016/j.ijhydene.2024.11.309.

[28] Wang, R., Zhang, B., Xia, Y., Wang, B., Zhang, S., Yue, W., Song, R.: Study on the hydrogen-air premixed flame propagation characteristics in semi-open space with obstacle. J. Loss Prev. Process Ind. 92, 105435 (2024a). https://doi.org/10.1016/j.jlp.2024.105435.

[29] Wang, T., Sheng, Y., Nan, F., Liu, L., Chen, J., Meng, F., Deng, J., Shi, J., Luo, Z.: Investigation on the flame and pressure behaviors of vented hydrogen-air deflagration from a duct-connected vessel: effects of venting diameter and static activation pressure. Energy 307, 132705 (2024b). https://doi.org/10.1016/j.energy.2024.132705.

[30] Xia, Y., Wang, B., Wang, X., Zhang, B., Zhang, S., Zhang, J., Shi, J., Ji, Y., Gong, Y.: Numerical investigation of hydrogen-air premixed flame evolution and explosion dynamics in obstructed space. Int. J. Hydrogen Energy 204, 153208 (2026). https://doi.org/10.1016/j.ijhydene.2025.153208.

[31] Xu, Z., Yang, G., Sheng, Z., Sun, H., Yang, X., Ji, S.: Large eddy simulation of premixed hydrogen-air combustion characteristics in closed space with different shrinkage rate. Int. J. Hydrogen Energy 81, 280–291 (2024). https://doi.org/10.1016/j.ijhydene.2024.07.212.

Supplementary Files

This is a list of supplementary files associated with this preprint. Click to download.

- FigS06terminaldotplot.tiff
- FigS05hydrodynamiccomparison.tiff
- ESM2onlineresource2meshrobustness.pdf
- FigS08aheadwindowrobustness.tiff
- FigS07frontdefinitionrobustness.tiff
- ESM1onlineresource1.pdf
- FigS10normalizedDb.tiff
- FTaCsourcedataandscriptsv01.zip
- FigS09wakewindowrobustness.tiff
- FigS11normalizeddp.tiff
- FigS03temperaturephi1p1.tiff
- FigS04velocityphi1p1.tiff
- FigS01temperaturephi0p9.tiff
- FigS02velocityphi0p9.tiff
- TableS03normalizedstagevalues.csv
- TableS04representativetimerobustnesssupport.csv
- TableS02thresholdsensitivity.csv
- TableS01eventonsetrobustness.csv
- FigS13.tif
- FigS12.tif
- FigS14.tif
- FigS15.tif
- TableS5.csv